Inventory of Supplementary Information

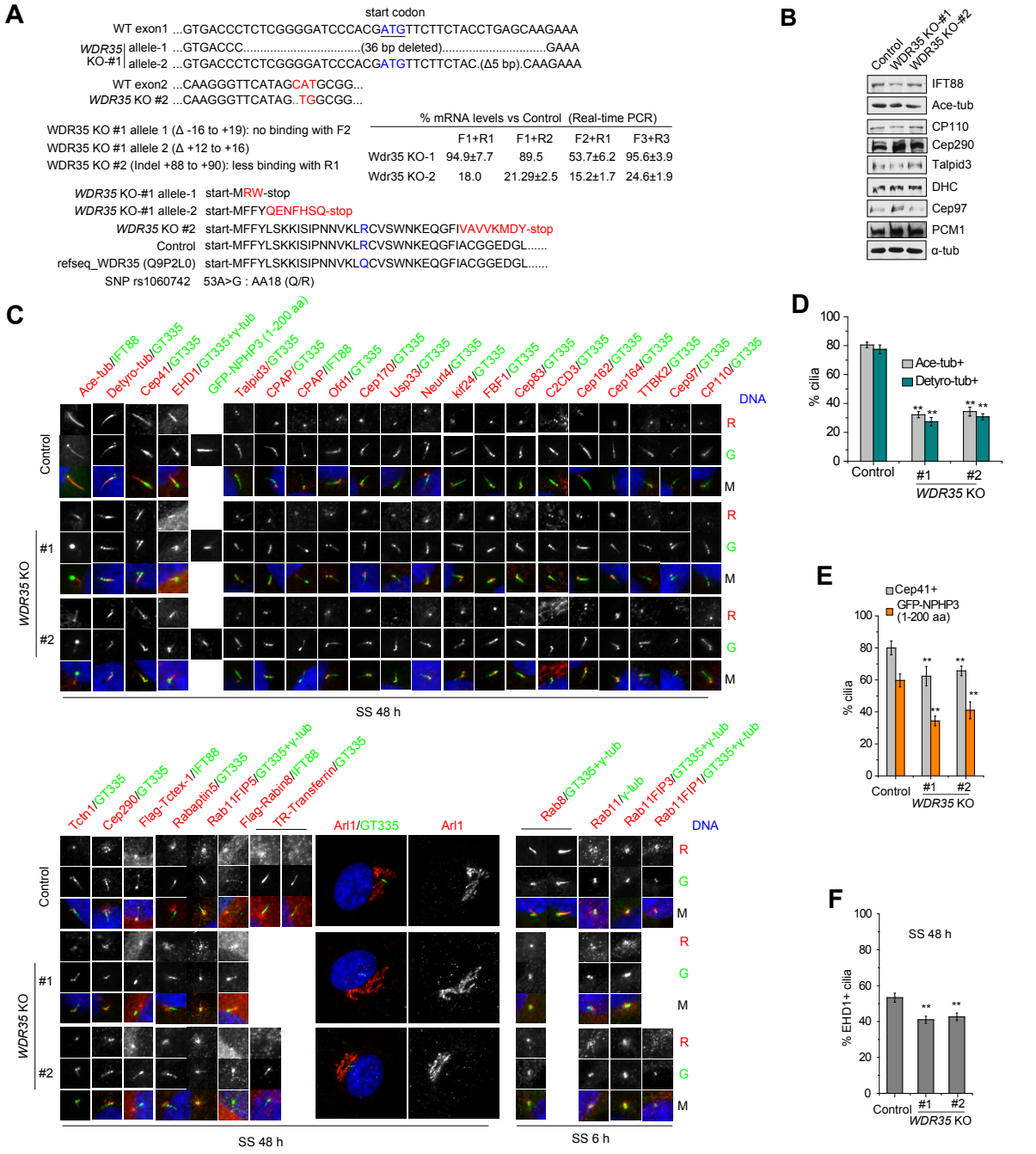

Figure S1. Characterization of *WDR35* KO clones reveals that Wdr35 specifically regulates a subset of cilium-related events. Related to Figure 1. (A) Generation of *WDR35* knockout (KO) RPE1 cells by CRISPR/Cas9. Single guide RNAs targeting exons 1 and 2 were used to generate two *WDR35* knock-out clones, #1 and #2. Sequence data for both alleles around the target region are shown. Knock-out clone #2 is homozygous for the indicated mutation. The mRNA levels of WDR35 were measured by real-time PCR and predicted translation products in control and *WDR35* knockout (KO) cells are based on verified genomic sequences. Different primers were used as indicated. Indels generated by CRISPR/Cas9 resulted in premature translation termination in both *WDR35* KO clones as shown. A Q18R polymorphism in Wdr35 protein, which was also found in SNP_rs1060742, exists in RPE1 cells used in this study. (B) Western blots of control and *WDR35* KO cell lysates were probed with indicated antibodies. DHC, cytoplasmic dynein 1 heavy chain 1; α-tubulin, loading control. (C) Representative images showing localization of various cilium and centriole markers in control and *WDR35* KO cells at 6 h and 48 h after serum starvation (SS), as indicated. Red (R), green (G), and merged (M) channels are indicated. (D) Percentages of cilia positive for acetylated (Ace-tub+) and detyrosinated tubulin (Detyro-tub+) in *WDR35* KO cells are shown. (E and F) Percentages of Cep41-, GFP-NPHP3 (1-200 aa)-, and EHD1-positive cilia as in (C) are shown. All data are presented as mean ± SD. $^{**}P < 0.01$.

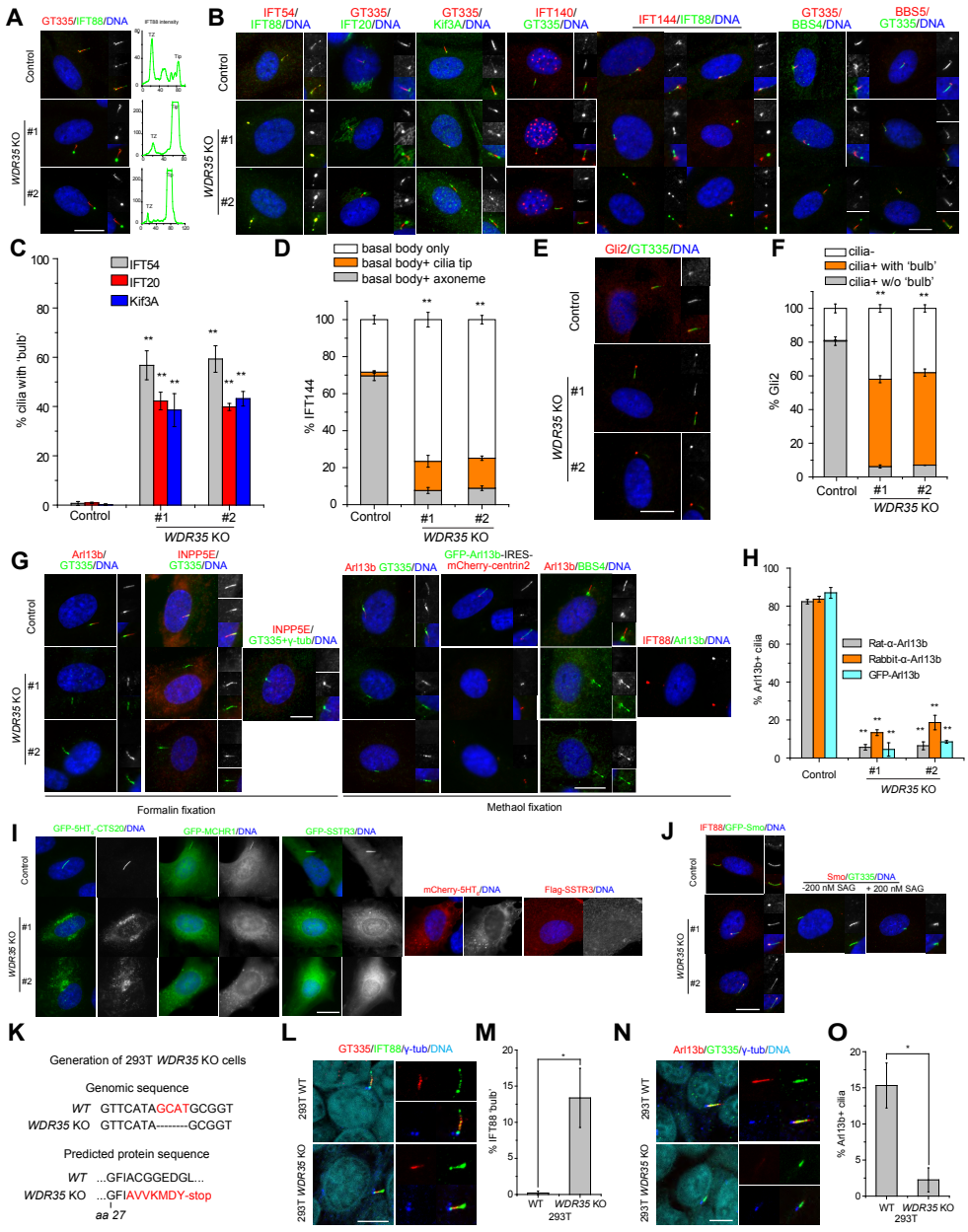

Figure S2. Wdr35 controls both retrograde transport inside cilia and membrane protein entry into cilia. Related to Figures 1 and 2. (A) Quantification of representative immunofluorescence images of control and *WDR35* KO cells stained with IFT88 and GT335. Distributions of IFT88 intensity (y-axis) along the primary cilium (x-axis, length in image pixels) are shown. TZ, transition zone. (B) Visualization of indicated proteins in *WDR35* KO. Each of these proteins showed aberrant strong accumulation inside cilia in *WDR35* KO cells, mostly at the tip, denoted as 'bulb' phenotype. (C) Percentages of cilia with 'bulb' phenotype as revealed by staining of IFT54, IFT20, and Kif3A. (D) Quantification of IFT144 phenotypes at cilia. Asterisks indicate significance of occurrence of bulbous IFT144. (E) Localization of Gli2 in *WDR35* KO. (F) Quantification of Gli2 localization phenotypes at cilia observed in (E). Asterisks indicate significance of occurrence of bulbous Gli2. (G) Ciliary membrane proteins (Arl13b and INPP5E) were visualized in serum-starved control and *WDR35* KO RPE1 cells. Representative images are shown. (H) Percentages of Arl13b-positive cilia in control and *WDR35* KO cells. Tests using two different antibodies against Arl13b, and lentiviruses expressing GFP-Arl13b-IRES-mCherry-centrin2 showed the same phenotype. (I) Representative images showing control and *WDR35* KO cells transfected with mCherry-5HT6, Flag-SSTR3, mCherry-5HT6-CTS20 or infected with retroviruses expressing GFP-MCHR1 or GFP-SSTR3. (J) Visualization of GFP-Smo and endogenous Smo in *WDR35* KO. (K) Generation of *WDR35* KO 293T cells by CRISPR/Cas9. Sequencing data are shown. (L, N) Representative images showing IFT88 (L) and Arl13b (N) in proliferating *WDR35* KO 293T cells under confluent conditions. (M, O) Percentages of cilia with IFT88 'bulb' and Arl13b-positive cilia observed in panels (L) and (N). Scale bar, 10 μm. All data are presented as mean ± SD. **P* < 0.05; ***P* < 0.01.

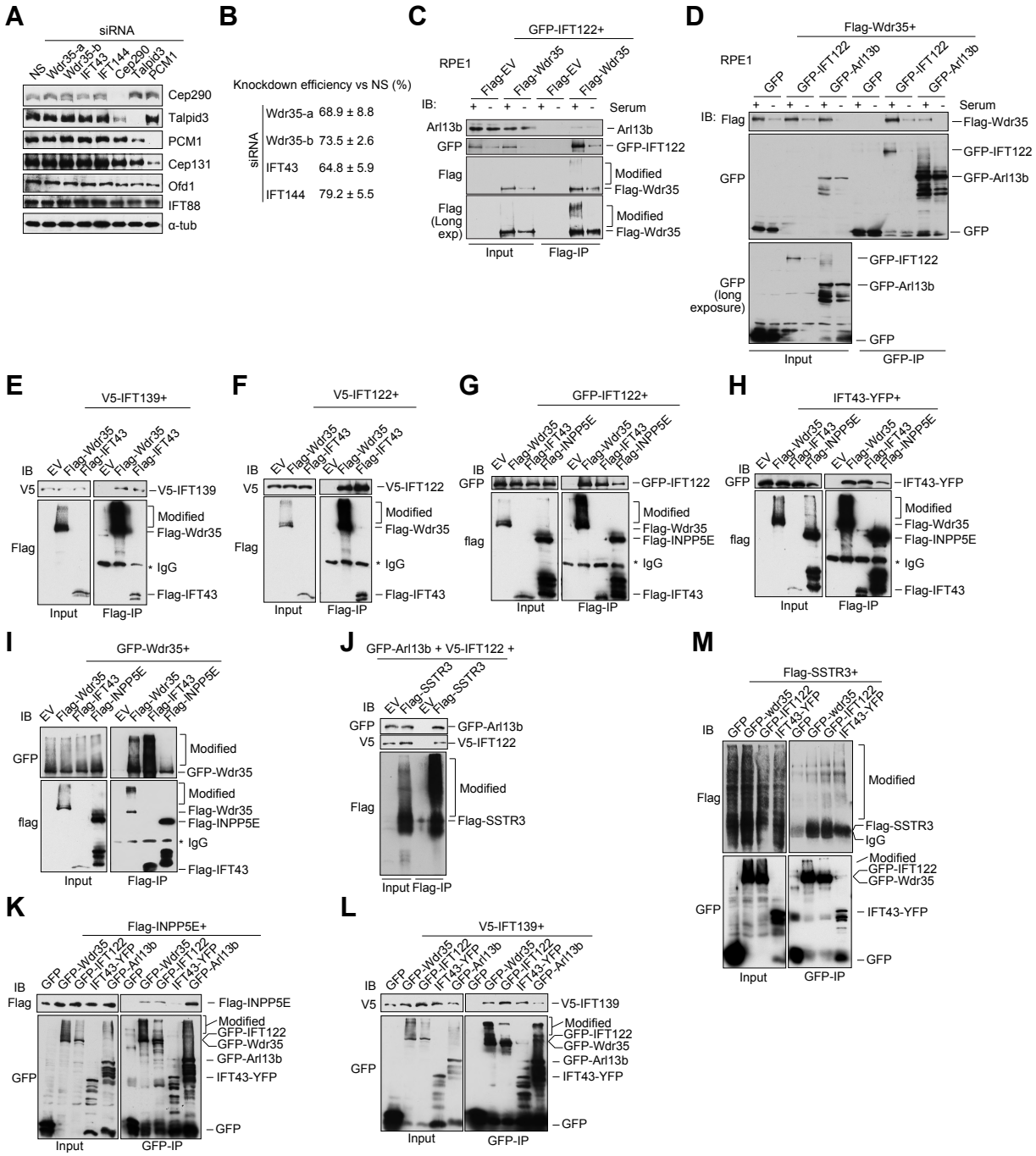

Figure S3. Wdr35 and other IFT-A subunits form a complex with ciliary membrane proteins. Related to Figure 3. (A) Western blots of extracts of RPE1 cells transfected with non-specific (NS) siRNAs and siRNAs targeting different IFT-A subunits (Wdr35, IFT43 and IFT144), Cep290, Talpid3, and PCM1 were probed using indicated antibodies. Two different Wdr35 siRNAs (a and b) were used. (B) Knock-down efficiency of IFT-A subunits was verified by quantitative real-time PCR. (C and D) Immunoprecipitations of RPE1 lysates showing interactions among two IFT-A subunits (Wdr35 and IFT122) and a ciliary membrane protein (Arl13b) under growing and serum-starved conditions. (E-M) Immunoprecipitations of 293T lysates showing interactions among four IFT-A subunits (Wdr35, IFT43, IFT122 and IFT139) and three ciliary membrane cargo proteins (Arl13b, INPP5E, and SSTR3). Lysates from cells transfected with different combinations of plasmids, as indicated, were immunoprecipitated using anti-Flag (C, E-J) and anti-GFP (D, L-M) antibodies. The identity of bands on the blots are indicated at right, and the smears indicate protein modifications, most likely ubiquitylation.

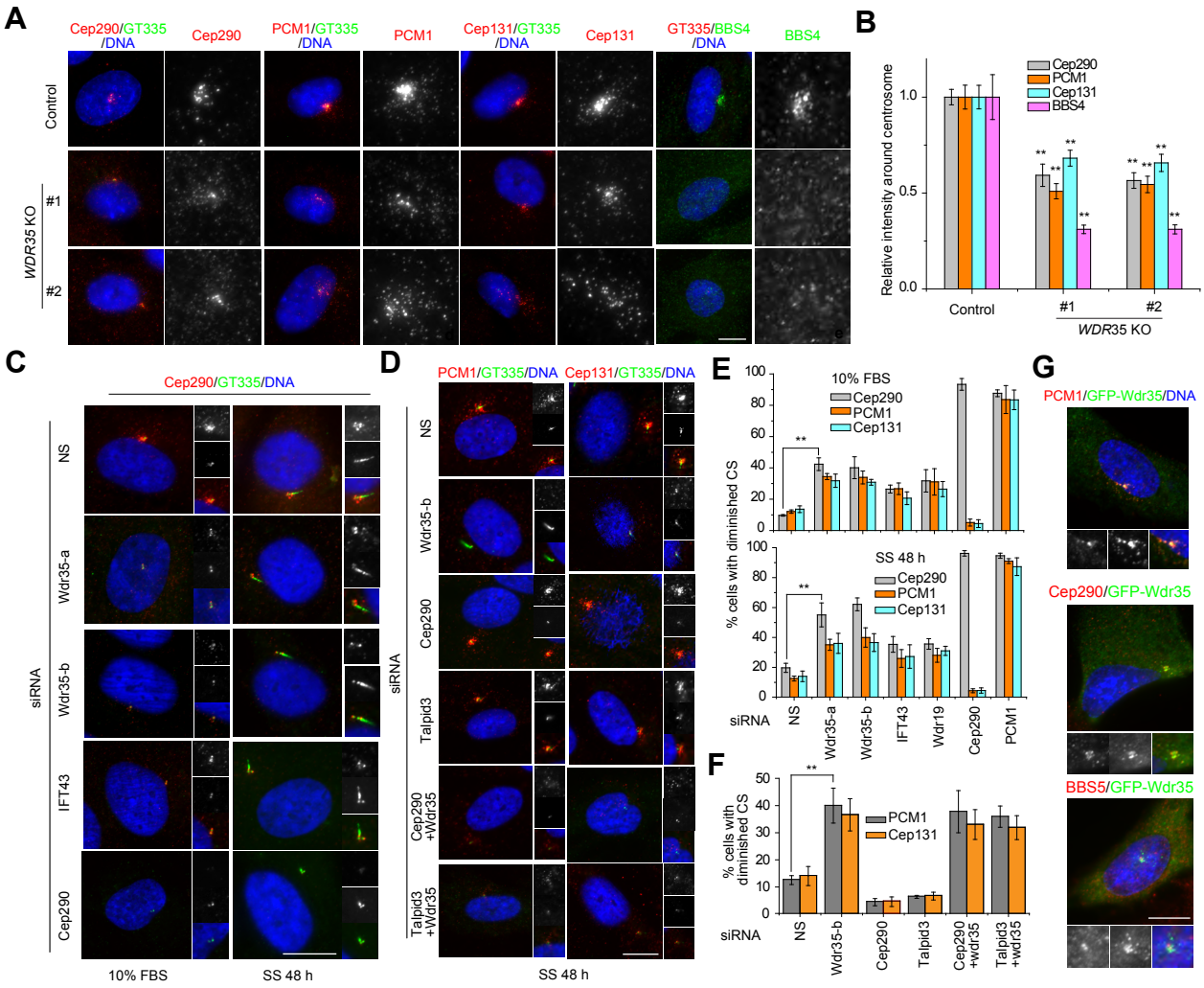

Figure S4. Wdr35 and IFT-A control centriolar satellite organization. Related to Figure 3. (A) Visualization of centriolar satellite proteins (Cep290, PCM1, Cep131, and BBS4) in control and *WDR35* KO RPE1 cells. (B) Quantification of the intensity of centriolar satellite proteins shown in (A). (C and D) Representative images of RPE1 cells transfected with siRNAs against indicated proteins. (E and F) Percentages of cells with dispersed centriolar satellites (stained with antibodies against Cep290, PCM1, or Cep131) in RPE1 cells treated with various siRNAs as indicated. (G) RPE1 cells transfected with GFP-Wdr35 were co-stained using antibodies against GFP and centrosomal proteins (PCM1, Cep290 and BBS5). Scale bar, 10 μm. Data are presented as mean ± SEM in (B), and mean ± SD in (E) and (F). $^{**}P < 0.01$.

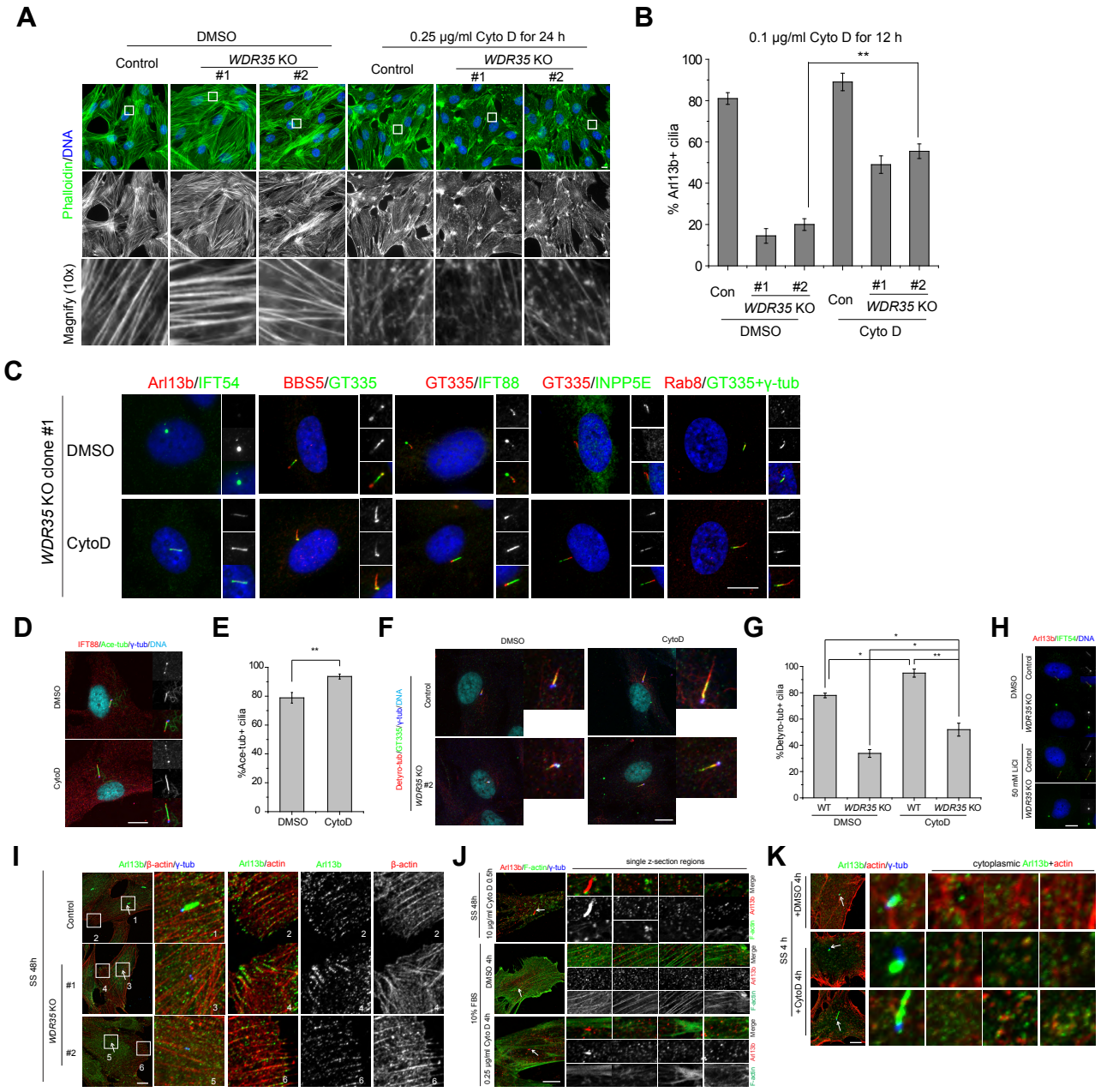

Figure S5. Wdr35-dependent membrane protein transport collaborates with the actin pathway. Related to Figures 4 and 5. (A) Visualization of F-actin by phalloidin in control and *WDR35* KO cells treated with DMSO or 0.25 μg/ml CytoD for 24 h. WDR35 ablation prevented Arl13b targeting to the cilium but not actin assembly. (B) Percentages of Arl13b-positive cilia in control and *WDR35* KO cells treated with either DMSO or 0.1 μg/ml CytoD for 12 h. (C) *WDR35* KO cells (clone-1) treated with DMSO or 0.25 μg/ml Cytochalasin D for 24h were visualized with antibodies against cilium markers, GT335, IFT54, IFT88, BBS5, and Arl13b. Representative immunofluorescence images are shown. (D-G) Control and *WDR35* KO cells treated with DMSO or Cytochalasin D for 24 h were visualized with antibodies against acetylated and detyrosinated tubulin. Quantifications of acetylated tubulin-positive (Ace-tub+) and detyrosinated tubulin-positive (Detyro-tub+) cilia are shown. (H) Wdr35-dependent transport is not rescued by LiCl. Control and *WDR35* KO cells were treated with 50 mM LiCl for 24 h. (I) Visualization of Arl13b together with β-actin in both control and *WDR35* KO cells 48 h post SS. (J and K) RPE1 cells in 10% FBS or serum starved for 4 h in the presence of DMSO or CytoD for 4 h were visualized as indicated. Co-localization of Arl13b with F-actin (J) or -actin (K) are shown. Arrows in (I-K) indicate centrosomes visualized by γ-tubulin. Scale bar, 10 μm.

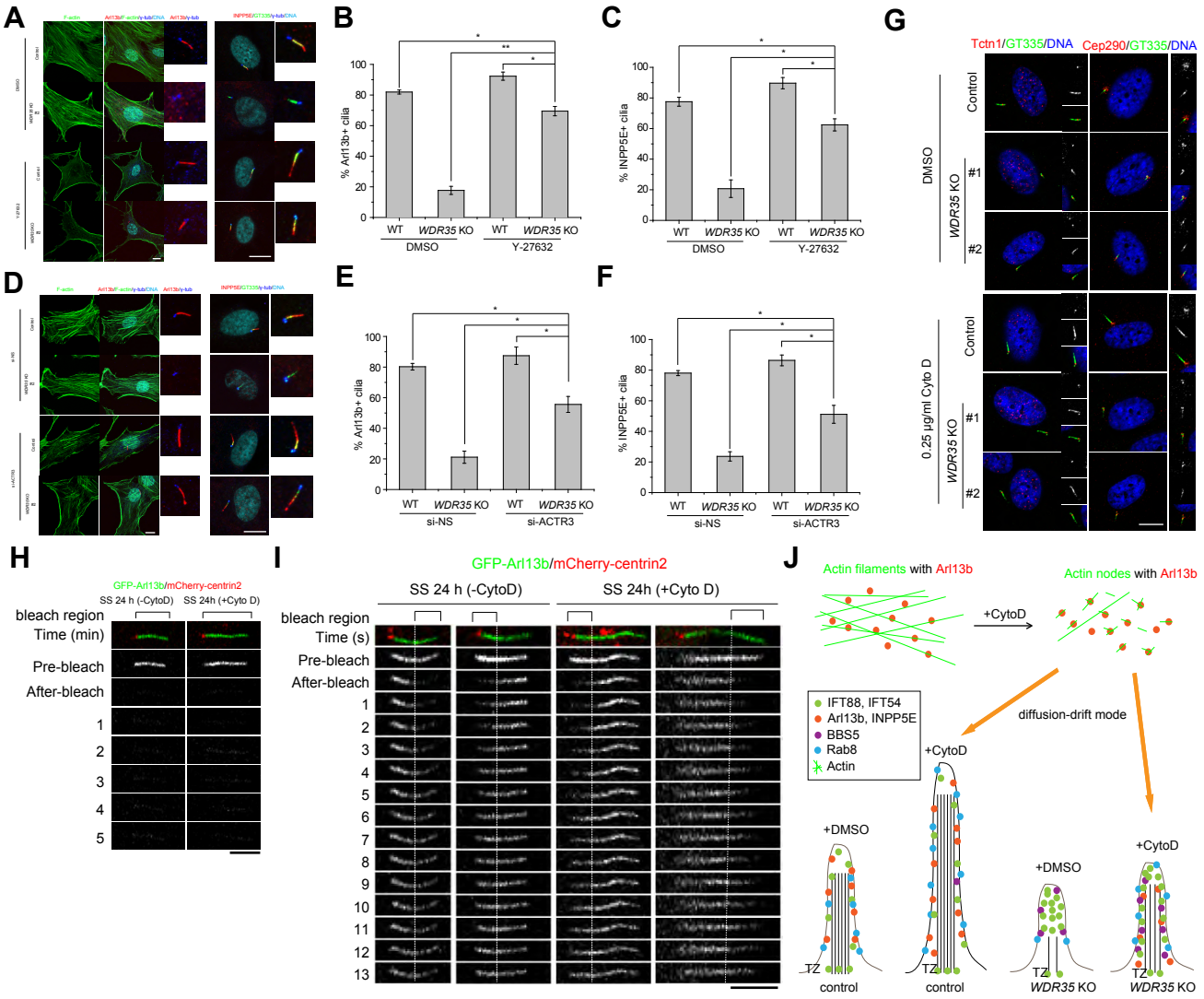

Figure S6. Destabilization of actin promotes the transport of Wdr35-regulated membrane cargoes to primary cilia. Related to Figures S5 and S6. (A) Control and *WDR35* KO cells treated with DMSO or Y-27632 for 24 h were visualized with antibodies against cilium markers. (B and C) Percentages of Arl13b+ and INPP5E+ cilia as in (A). (D) Visualization of F-actin and cilia in control and *WDR35* KO cells transfected with non-specific siRNAs or siRNAs against ACTR3. (E and F) Percentages of Arl13b+ and INPP5E+ cilia as in (D). (G) Control and *WDR35* KO cells treated with DMSO or 0.25 μg/ml Cytochalasin D for 24 h were visualized with antibodies against transition zone markers, Cep290 and Tctn1. (H) FRAP of GFP-Arl13b was observed after bleaching the entire cilium without or with CytoD treatment. (I) FRAP of GFP-Arl13b in proximal and distal regions of the cilium without or with CytoD treatment. Both proximal and distal regions of cilia were bleached as indicated, and recovery was observed for the indicated time points. Scale bars in (A), (D) and (G), 10 μm; Scale bars in (H) and (I), 5 μm. (J) Schematic showing cargo distribution in *WDR35* KO before and after actin depolymerization by CytoD treatment. CytoD treatment releases Arl13b from actin bundles to form numerous Arl13b-actin nodes, which further target to the centrosome and cilium through diffusion-drift mode. Besides Arl13b, cilium targeting of INPP5E, Rab8, and BBS5 is enhanced by CytoD. In control cells, IFT-B components (IFT88 and IFT54) and membrane protein Arl13b are normally distributed inside cilia, and BBsome subunit BBS5 is rapidly exported from cilia. In control cells with Cytochalasin D, elongated cilia are formed and enhanced ciliogenesis further promotes entry of all ciliary cargoes. In *WDR35* KO cells, because retrograde intraflagellar transport, cargo exit, and membrane protein entry are compromised, primary cilia are enriched with IFT-B and BBsome but lack certain membrane proteins. Actin depolymerization rescues the Arl13b and INPP5E entry defects caused by Wdr35 ablation. In turn, cilium-targeted membrane proteins like Arl13b associate with IFT-B and partially diminish the IFT-B 'bulb' through diffusion or transport. However, cilia length and exit defects are not rescued, so IFT-B and BBsome remain concentrated within cilia. TZ, transition zone.

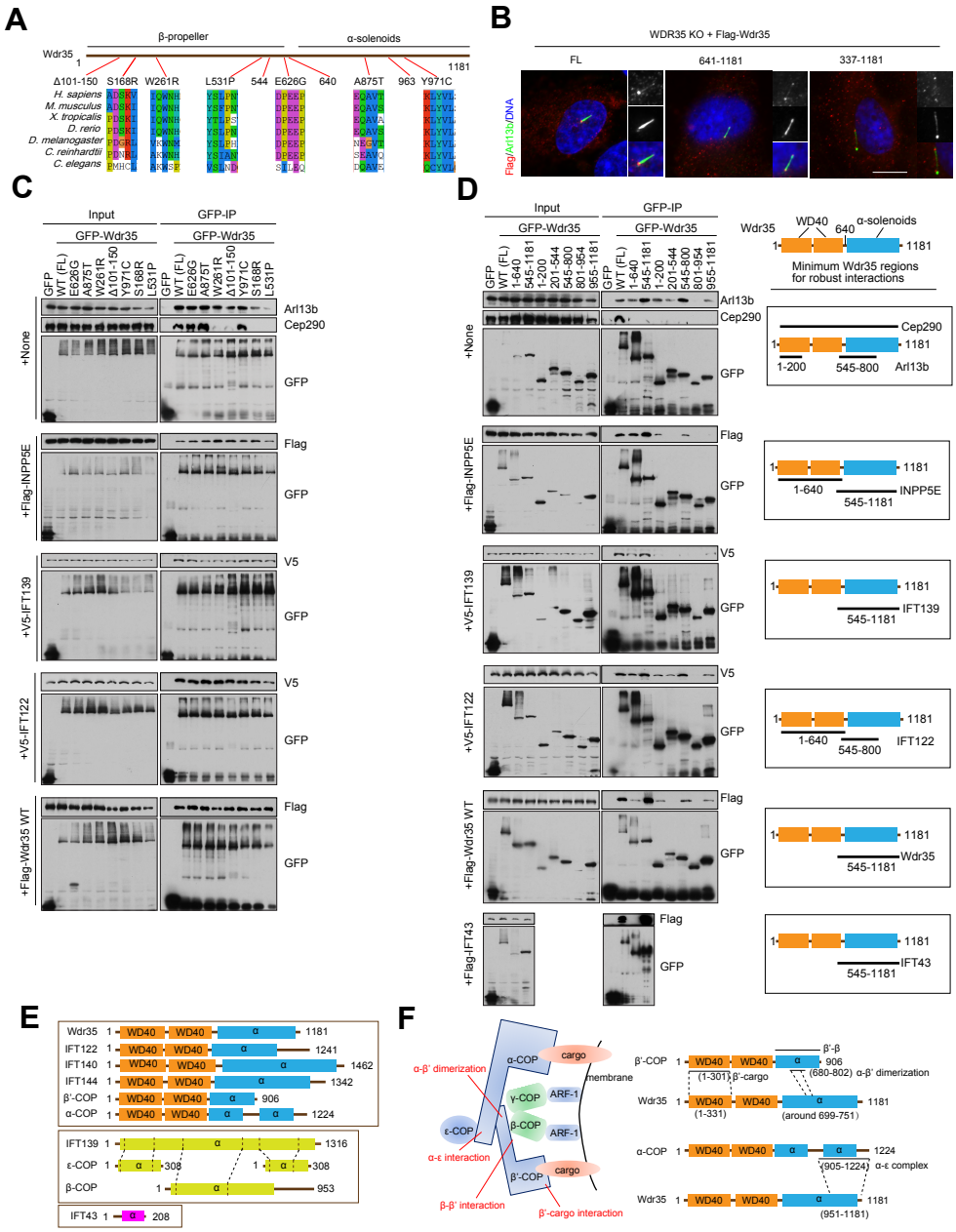

Figure S7. Wdr35 disease-related mutants show variable defects, and Wdr35-containing IFT-A complex may adopt a COPI-like structure for transport. Related to Figure 6. (A) Schematic showing domains of human Wdr35 protein and conservation among species. The Wdr35 mutants used in this study are labeled. The regions surrounding the disease-related mutation site are highly conserved among different species as shown. (B) Representative images showing *WDR35* KO cells expressing full-length Wdr35 and C-terminal Wdr35 truncations. Scale bar, 10 μm. (C) Anti-GFP immunoprecipitations of lysates of 293T cells co-expressing GFP-tagged Wdr35 mutants alone or with Flag-INPP5E, V5-IFT139, V5-IFT122, or Flag-Wdr35 as indicated. The inputs and immunoprecipitates were probed as shown. (D) Anti-GFP immunoprecipitations of lysates of 293T cells expressing GFP-tagged Wdr35 truncations alone or with Flag-INPP5E, V5-IFT139, V5-IFT122, Flag-Wdr35, or Flag-IFT43 as indicated. Minimal Wdr35 regions required for interactions with indicated proteins are illustrated. (E) Predicted secondary structures of Wdr35 and other IFT-A subunits aligned with subunits of the COPI coat complex. Four IFT-A subunits (Wdr35, IFT122, IFT140 and IFT144) resemble α-COP and β'-COP with two N-terminal WD40 β-propeller folds and C-terminal α-solenoids. IFT139 shows similarity with β-COP and ε-COP with long TPR repeats, whereas homolog in COPI is not found for IFT43 with α-helix structure. (F) Schematic showing COPI topology and interaction network (*left*) and alignment of homologous regions in COPI and Wdr35 (*right*). (*Left*) In COPI, α- and β'-COP dimerize using their α-solenoids to form an arch-like structure over β- and γ-COP. Two N-terminal WD40-regions of α- and β'-COP directly bind to membrane cargoes, and β- or γ-COP binds the membrane indirectly through a small GTPase, Arf1. (*Right*) Regions in α- and β'-COP required for α-β', α-ε, β-β', and β'-cargo interactions were aligned with Wdr35.

Figure 2L

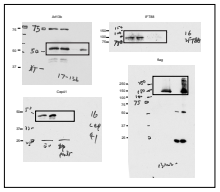

Figure 3E

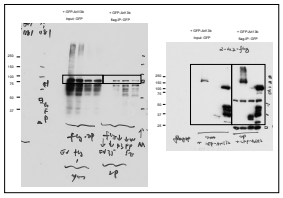

Figure 3F

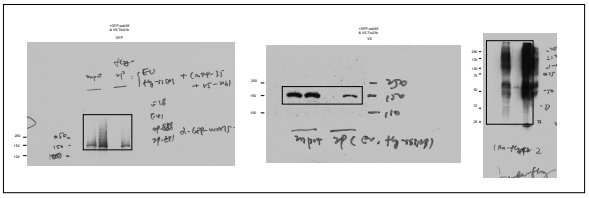

Figure 3G

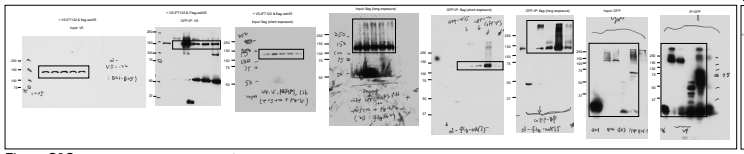

Figure S1B

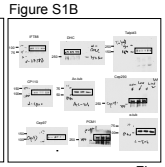

Figure S3A

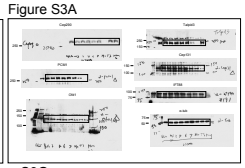

Figure S3C

Figure S3D

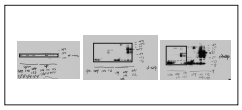

Figure S3E

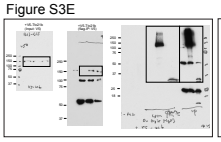

Figure S3F

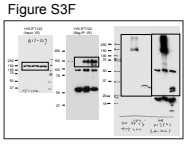

Figure S3G

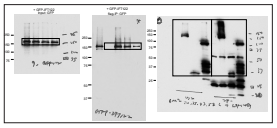

Figure S3H

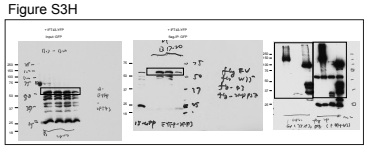

Figure S3I

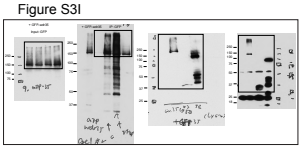

Figure S3J

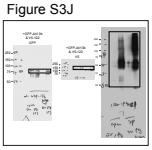

Figure S3K

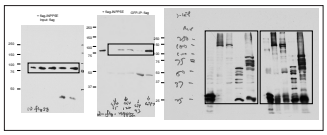

Figure S3L

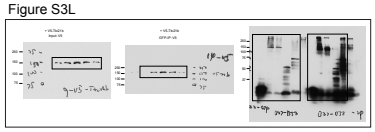

Figure S7C (+None)

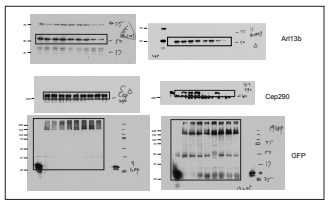

Figure S7C (+Flag-INPP5E)

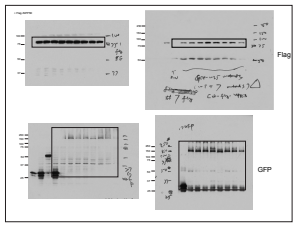

Figure S3M

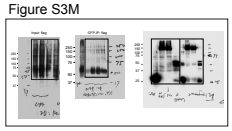

Figure S7C (+V5-IFT139)

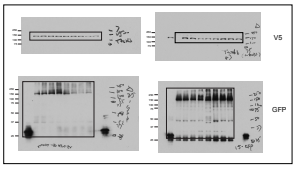

Figure S7C (+V5-IFT122)

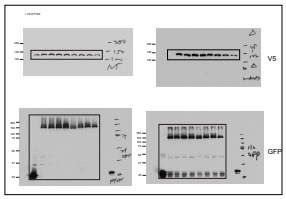

Figure S7C (+Flag-Wdr35 WT)

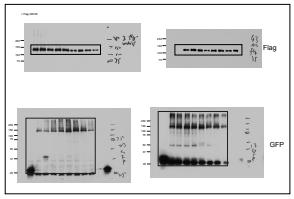

Figure S7D (+None)

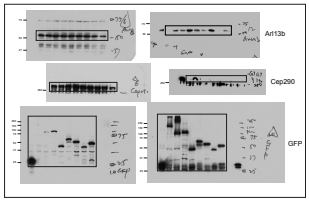

Figure S7D (+Flag-INPP5E)

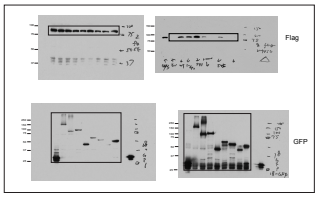

Figure S7D (+V5-IFT139)

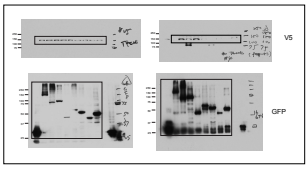

Figure S7D (+V5-IFT122)

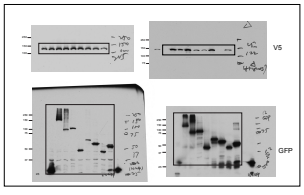

Figure S7D (+Flag-Wdr35 WT)

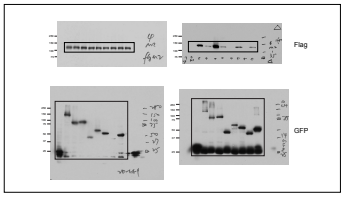

Figure S7D (+Flag-IFT43)

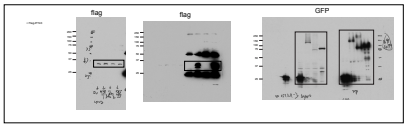

Figure S8. Uncropped western blots.

Table S1. Summary of the role of Wdr35 in regulation of centrosome and cilium-related proteins. Related to Figures 1, 2, S1 and S2.

	Genes/Proteins	Test methods in this study	Defects observed in *WDR35* KO	Protein annotations	Fixation method
1	GT335	endogenous	decrease of modifications at cilium	tubulin glutamylation	Methanol
2	Ace-tub	endogenous	decrease of modifications at cilium	tubulin acetylation	Methanol
3	Detyro-tub	endogenous	decrease of modifications at cilium	tubulin detyrosylation	Methanol
4	IFT88	endogenous	retrograde IFT defects, percentage of cilia slightly reduced	IFT-B subunit	Methanol
5	IFT54	endogenous	retrograde IFT defects, percentage of cilia slightly reduced	IFT-B subunit	Methanol
6	IFT20	endogenous	retrograde IFT defects, percentage of cilia slightly reduced, Golgi body not affected	IFT-B subunit, golgi body	Methanol
7	Kif3A	endogenous	retrograde IFT defects, percentage of cilia slightly reduced	kinesin, cilium anteograde motor	Methanol
8	IFT140	endogenous	retrograde IFT defects, percentage of cilia slightly reduced	IFT-A subunit	Methanol
9	IFT144	endogenous	cilium entry and retrograde transport defects	IFT-A subunit	Methanol
10	BBS4	endogenous	retrograde IFT defects, cilium exit defects, partially dispersed centriolar satellites	BBSome subunits, centriolar satellites	Methanol
11	BBS5	endogenous	retrograde IFT defects, cilium exit defects	BBsome subunits	Methanol
12	Gli2	endogenous	retrograde transport defects, percentage of cilia slightly reduced	Hedgehog transcription factor	Methanol
13	Arl13b	endogenous	strong cilium entry defects, weak retrograde IFT defects	membrane, ADP-ribosylation factor-like protein 13B	Both
14		GFP-Arl13b-IRES-mCherry-Centrin-2	cilium entry defects	membrane, ADP-ribosylation factor-like protein 13B	Methanol
15	INPP5E	endogenous	strong cilium entry defects, weak retrograde IFT defects	membrane, inositol polyphosphate-5-phosphatase E	Both
16	5HT6	mCherry-5HT6	cilium entry defects	GPCR, serotonin receptor	Forrmalin
17		GFP-5HT6-CTS20	cilium entry defects	GPCR, 5HT6 linked with an CTS sequence	Forrmalin
18	SSTR3	Flag-SSTR3	cilium entry defects	GPCR, somatostatin receptor type 3	Forrmalin
19		GFP-SSTR3	cilium entry defects	GPCR, somatostatin receptor type 3	Forrmalin
20	MCHR1	GFP-MCHR1	cilium entry defects	GPCR, melanin-concentrating hormone receptor 1	Forrmalin
21	Smo	endogenous	strong cilium entry defects, weak retrograde IFT defects	GPCR, Hh-dependent cilium entry	Forrmalin
22		GFP-Smo	retrograde IFT defects, percentage of cilia slightly reduced	GPCR, cilium entry not relying on Hh	Methanol
23	PCM1	endogenous	partially dispersed centriolar satellites	centriolar satellites	Methanol
24	Cep131	endogenous	partially dispersed centriolar satellites	centriolar satellites	Methanol
25	Cep290	endogenous	partially dispersed centriolar satellites, transition zone localization not affected	centriolar satellites, transition zone	Methanol
26	Rab8	endogenous	Strong defects in growth and remodeling at the cilium, weak defects in initial docking	cilium vesicle	Formalin
27	NPHP3	GFP-NPHP3 (1-200aa)	percentage of cilia slightly reduced	inversin compartment	Forrmalin
28	Cep41	endogenous	percentage of cilia slightly reduced	tubulin glutamylation	Methanol
29	EHD1	endogenous	percentage of cilia slightly reduced	cilium pocket	Forrmalin
30	TTBK2	endogenous	no defect observed	mother centriole loading during early ciliogeneiss, transition zone	Methanol
31	CP110	endogenous	no defect observed	centriole, removed from mother centriole during initiation of cilia assembly	Methanol
32	Cep97	endogenous	no defect observed	centriole, removed from mother centriole during initiation of cilia assembly	Methanol
33	Rab11FIP1	endogenous	no defect observed	RAB11 Family Interacting Protein 1	Forrmalin
34	Rab11FIP3	endogenous	no defect observed	RAB11 Family Interacting Protein 3	Forrmalin
35	Rab11FIP5	endogenous	no defect observed	RAB11 Family Interacting Protein 5	Forrmalin
36	Rabin8	Flag-Rabin8	no defect observed	vesicle-related	Forrmalin
37	Rabaptin 5	endogenous	no defect observed	vesicle-related	Forrmalin
38	Rab11	endogenous	no defect observed	vesicle-related	Forrmalin
39	Talpid3	endogenous	no defect observed	centrosome/centriole/basal body	Methanol
40	CPAP	endogenous	no defect observed	centrosome/centriole/basal body	Methanol
41	Ofd1	endogenous	centriole localization not affected	centrosome/centriole/basal body/centriolar satellites	Methanol
42	Cep170	endogenous	no defect observed	centrosome/centriole/basal body	Methanol
43	Usp33	endogenous	no defect observed	centrosome/centriole/basal body	Methanol
44	Neul4	endogenous	no defect observed	centrosome/centriole/basal body	Methanol
45	Kif24	endogenous	no defect observed	centrosome/centriole/basal body	Methanol
46	FBF1	endogenous	no defect observed	centrosome/centriole/basal body	Methanol
47	Cep83	endogenous	no defect observed	centrosome/centriole/basal body	Methanol
48	C2CD3	endogenous	no defect observed	centrosome/centriole/basal body	Methanol
49	Cep162	endogenous	no defect observed	centrosome/centriole/basal body	Methanol
50	Cep164	endogenous	no defect observed	centrosome/centriole/basal body	Methanol
51	Tctex-1	Flag-Tctex-1	no defect observed	centrosome/centriole/basal body	Methanol
52	Arl1	endogenous	no defect observed	golgi	Methanol
53	β-catenin	endogenous	adhesive junction localization not affected	adhesive junction, wnt signaling	Methanol
54	Transferrin	Texas-red-transferrin uptake	no defect observed	endocytosis	Forrmalin
55	Tctn1	endogenous	no defect observed	transition zone	Methanol
56	F-actin	FITC-Phalloidin	no defect observed	F-actin network	Forrmalin
57	β-actin	endogenous	no defect observed	total actin	Methanol

Table S2. Summary of interactions and functional properties of Wdr35 mutants. Related to Figures 6 and S7.

	Arl13b	INPP5E	Ttc21b	IFT122	Wdr35 WT	IFT43	Cep290	Cilium targeting	retrograde IFT rescue	Arl13b entry rescue
FL WT	***	***	***	***	***	***	***	***	***	***
E626G	***	***	***	***	***	N.T.	***	***	***	***
A875T	***	***	**	***	***	N.T.	***	*	*	*
W261R	***	***	**	***	***	N.T.	*/-	*	*	*
Δ101-150	***	***	**	***	***	N.T.	*/-	*	*	*
Y971C	***	***	***	***	***	N.T.	***	*	*	*
S168R	**	***	***	***	***	N.T.	-	*	*	*
L531P	*	**	***	**	***	N.T.	-	*	*	*
1-640	***	***	*	**	*/-	-	-	-	-	-
545-1181	***	***	***	***	***	***	-	N.T.	N.T.	N.T.
1-200	***	*	*/-	*	*/-	N.T.	-	N.T.	N.T.	N.T.
201-544	*	-	-	*	-	N.T.	-	N.T.	N.T.	N.T.
545-800	***	*	*/-	***	*	N.T.	-	N.T.	N.T.	N.T.
801-954	-	-	-	-	-	N.T.	-	N.T.	N.T.	N.T.
955-1181	*	-	*/-	*	*/-	N.T.	-	N.T.	N.T.	N.T.
1-963	N.T.	N.T.	N.T.	N.T.	N.T.	N.T.	N.T.	**	*/-	*
641-1181	N.T.	N.T.	N.T.	N.T.	N.T.	N.T.	N.T.	***	**	**
337-1181	N.T.	N.T.	N.T.	N.T.	N.T.	N.T.	N.T.	***	*	**

***, strong; **, medium; *, weak; -, negative. N.T., not tested.

Supplemental Movies 1-4

Movie S1. Live-cell imaging of wild-type RPE1 cells expressing GFP-Arl13b-IRES-mCherry-centrin2 after serum starvation without Cytochalasin D. Related to Figure 5.

Movie S2. Live-cell imaging of wild type RPE1 cells expressing GFP-Arl13b-IRES-mCherry-centrin2 after serum starvation with Cytochalasin D. Related to Figure 5.

Movie S3. Live-cell imaging of *WDR35* KO RPE1 cells expressing GFP-Arl13b-IRES-mCherry-centrin2 after serum starvation without Cytochalasin D. Related to Figure 5.

Movie S4. Live-cell imaging of *WDR35* KO RPE1 cells expressing GFP-Arl13b-IRES-mCherry-centrin2 after serum starvation with Cytochalasin D. Related to Figure 5.

Supplemental Discussion

Topological parallels between IFT-A and COPI complexes

Here, we have provided evidence for the role of Wdr35 and the entire IFT-A complex in transport of proteins to the primary cilium. It has been suggested that IFT-A proteins evolved from a proto-coatomer (Jekely and Arendt, 2006; Taschner et al., 2012). Computational modeling of Wdr35 interactions within the mammalian IFT-A complex lends credence to this hypothesis. First, amino acid sequence and secondary structure predictions suggest that four IFT-A subunits (Wdr35, IFT122, IFT140 and IFT144) are homologous to *α* and *β'* subunits of coat complex, COPI (Avidor-Reiss et al., 2004; Mill et al., 2011; van Dam et al., 2013), and α-helical regions of IFT139 are structurally homologous to *β*- and *ε*-COP (Figure S7E). Different subunits of COPI form a large complex to bind membranes and transport cargoes, and the *α-β'-β-γ-ε*-Arf1-cargo complex with membrane has been structurally resolved (schematized in Figure S7F) (Dodonova et al., 2015; Lee and Goldberg, 2010). *α*- and *β'*-COP directly bind to membrane cargo and indirectly bind with membrane through *β'*-COP. We therefore aligned regions in *α*- and β'-COP that are required for COPI complex formation and cargo binding with Wdr35 to predict subunit interacting and cargo binding sites in Wdr35 (Figure S7F). Different regions in Wdr35 were found to be homologous to regions in *α*- and β'-COP with respect to *α-β'*, *α-ε, β-β',* and *β*'-cargo interactions (Figures 6D-E and S7F). Interestingly, our mapping studies experimentally verified several homology-based predictions regarding IFT-A complex formation and IFT-A-cargo binding (Figures 6E-F). Given that multiple IFT-A subunits form a large complex able to interact with and transport cargoes, like COPI (Figure 3H), and given the similarities between interactions within IFT-A and COPI, we suggest that the overall architecture of IFT-A with cargoes could recapitulate the COPI complex. Future higher-resolution structural studies and structure-function experiments will be required to test this model as well as the impact of ciliopathy-related mutations on the overall IFT-A complex.

Subunits within IFT-A play diverse roles

In an *IFT144* mutant, but not in *IFT122* null MEFs, Arl13b, ACIII, and Smo were depleted from cilia (Liem et al., 2012). Furthermore, although our study indicated that retrograde transport and exit of BBS4 and BBS5 were blocked in *WDR35* KO cells, cilium entry of the BBSome is blocked in a *C. elegans dyf-2* (*IFT144*) mutant (Wei et al., 2012). In *Chlamydomonas*, BBS4 is moved by IFT (Lechtreck et al., 2009) and is elevated in *dhc1b-2* and *fla17-1* (*IFT139* mutant) strains but not in *fla15-1* (*IFT144* mutant) cilia (Lechtreck et al., 2013). Moreover, the BBsome was identified as a bona fide constituent of IFT in olfactory sensory neurons (Williams et al., 2014), which may suggest differences in BBS4 transport and exit across species. Moreover, the diverse phenotypes obtained with different IFT-A subunit mutants and persistent interactions observed after depletion of a single subunit (Behal et al., 2012; Mukhopadhyay et al., 2010) could suggest that distinct IFT-A sub-complexes form or that IFT-A subunits have both overlapping and unique functions.

Wdr35 was previously proposed to be a peripheral rather than a 'core' component of IFT-A, and its knock-down by siRNAs showed very weak retrograde IFT defects and little effect on cilium targeting of GFP-SSTR3 (Mukhopadhyay et al., 2010). However, in our studies, *WDR35* gene ablation led to severe retrograde IFT defects, and SSTR3 was not targeted to cilia in *Wdr35* KO cells. These differences could be

explained by the use of diverse gene ablation approaches or other technical differences. Additionally, during evolution, IFT139 and/or IFT43, but not Wdr35, is lost in some species (van Dam et al., 2013), suggesting that Wdr35 indeed plays a key role in IFT-A function. Interestingly, different COPI subunits were found to bind cargoes through distinct but overlapping sets of di-lysine motifs (Eugster et al., 2004). Considering the similarity with COPI, IFT-A might also use distinct subunits to bind and transport membrane proteins. Future studies, with cells harboring mutations in multiple subunits, will be needed to resolve the function and potential heterogeneity of IFT-A sub-complexes, if they exist.

IFT-A Cargo specificity

Specific transport of cargoes (e.g., Gpr161) into the cilium relies on consensus sequences (Bhogaraju et al., 2013; Mukhopadhyay et al., 2013), but future studies are needed to understand how IFT-A specifically recognizes and transports its diverse cargoes. Additionally, cargoes of IFT-A were found to be transported by IFT-B, the BBSome machinery (Cevik et al., 2013; Jin et al., 2010), and other pathways (Gotthardt et al., 2015; Wright et al., 2011), but how these cargoes engage the correct pathway is unknown. Interestingly, loss of INPP5E has been shown to recruit Tulp3 and IFT-A to cilia, implying reciprocal feedback control between IFT-A and membrane proteins (Chavez et al., 2015; Garcia-Gonzalo et al., 2015). Findings described here and other observations showing that the IFT-A complex plays cilium-independent roles (Balmer et al., 2015) help broaden our understanding of the non-ciliary functions of this complex.

Supplemental Experimental Procedures

Plasmids

pCMV5-Flag-Wd35 was used to express Flag-tagged Wdr35. Wdr35 wild-type and fragments were amplified by PCR and sub-cloned into pEGFP vectors to generate GFP-tagged Wdr35 constructs. Wdr35 mutants were generated by site-directed mutagenesis. In rescue experiments, wild-type Wdr35 and mutants were cloned into a modified pLVX-3xFlag-IRES-puromycin lentiviral vector. The lentiCas9-Blast (Addgene #52962) plasmid was used to express Flag-tagged Cas9 and lentiGuide-Puro (Addgene #52963) to express guide RNAs (Sanjana et al., 2014). $5HT_6$-mCherry and $5HT_6$-GFP-CTS20 were gifts from T. Inoue (Su et al., 2013), Flag-SSTR3 was a gift from M. von Zastrow (Leaf and Von Zastrow, 2015). Flag-INPP5E was a gift from S. Seo (Humbert et al., 2012). pBabe-GFP-SSTR3, pBabe-GFP-MCHR1 and pLAP7-NPHP3 (1-200 aa) (GFP-tagged) were gifts from P.K. Jackson (Mukhopadhyay et al., 2010; Wright et al., 2011). Flag-Rabin8 was from K. Mizuno and S. Chiba (Chiba et al., 2013). EGFP-Smo was a gift from J.F. Reiter (Corbit et al., 2005; Wu et al., 2012), Flag-Tctex-1 was generated by sub-cloning of Tctex-1 cDNA (Open Biosystems) into pLVX-3xFlag-IRES-puro vector. pEGFP-C2-Arl13b was a gift from T. Katada (Hori et al., 2008), and pLVX-GFP-Arl13b-mCherry-Centrin2 was generated by sub-cloning. pEGFP-C1-IFT122 and V5-IFT122 were gifts from J. Eggenschwiler (Qin et al., 2011). pCAGIG-V5-IFT139 was a gift from E.E. Davis and N. Katsanis (Davis et al., 2011). IFT43-EYFP and CTAP-IFT43 (Flag-tagged) were gifts from H.H. Arts and R. Roepman (Arts et al., 2011). All PCRs for sub-cloning were performed using high fidelity PfuTurbo or Herculase II Fusion DNA polymerases (Agilent), and the PCR-generated plasmids were further verified by DNA sequencing.

Antibodies

The antibodies used, and their dilutions for western blotting (WB) and immunofluorescence (IF) are as follows. Rabbit anti-Flag (1:2000 for WB, F7425, Sigma), mouse anti-Flag (1:2000 for WB and 1:500 for IF, F1804, Sigma), mouse anti-V5 (1:2000 for IF, R960-25, Invitrogen), rabbit anti-GFP (1:2000 for WB, G1544, sigma), mouse anti-GFP (1:500 for IF, 11814460001, Roche), mouse anti-GFP (DSHB-GFP-8H11, Hybridoma bank), mouse anti-α-tubulin (1:5000 for WB, T5168, Sigma), rabbit anti-cytoplasmic dynein 1 heavy chain 1 (Dync1h1) (1:1000 for WB, sc-9115, SantaCruz), rabbit anti-γ-tubulin (1:2000 for IF, T5192, sigma), mouse anti-γ-tubulin (1:1000 for IF, T5326 and T6557, sigma), goat anti-γ-tubulin (1:500 for IF, sc-7396, SantaCruz), mouse anti-polyglutamylated tubulin (GT335) (1:2500 for IF, AG-20B-0020-C100, Adipogen), mouse anti-acetylated tubulin (clone 6-11-B1, 1:2000 for WB and 1:1000 for IF, T7451, Sigma), rabbit anti-detyrosinated tubulin (1:500 for IF, AB3201, Chemicon), rabbit anti-IFT88 (1:1000 for WB and 1:500 for IF, 13967-1-AP, Proteintech), mouse-anti-IFT54 (1:500 for IF, ab68958, Abcam), rabbit anti-IFT20 (1:500 for IF, 13615-1-AP, Proteintech), rabbit anti-Kif3A (1:200 for IF, K3513, Sigma), rabbit anti-IFT140 (1:200 for IF, 17460-1-AP, Proteintech), mouse anti-IFT144 (1:100 for IF, H00057728-B01P, Abnova), rabbit anti-BBS4 (1:500 for IF, gift from K. Rhee (Kim et al., 2012)), rabbit anti-Rab11FIP1, Rab11FIP3 and Rab11FIP5 (1:200 for IF, gift from R. Prekeris (Prekeris, 2015)), rabbit anti-BBS5 (1:500 for IF, 14569-1-AP, Proteintech), rabbit anti-Gli2 (1:200 for IF, sc-28674, SantaCruz), rat-anti-Arl13b (1:100 for IF, gift from T. Katada and K. Kontani), rabbit anti-Arl13b (1:2000 for WB and 1:2000 for IF, 17711-1-AP, Proteintech), rabbit anti-INPP5E (1:500 for IF, 17797-1-AP, Proteintech), rabbit anti-Smoothened (1:200 for IF, ab38686, Abcam), rabbit anti-PCM1 (1:1000 for WB and 1:500 for IF, sc-67204, SantaCruz), rabbit anti-Cep131 (1:1000 for WB and 1:500 for IF, A301-415A, Bethyl), rabbit anti-Cep290 (1:1000 for WB and 1:500 for IF, A301-659A, Bethyl), rabbit anti-Rab8 (1:200 for IF, gift from J. Peränen (Hattula et al., 2006)), rabbit anti-Cep41 (1:1000 for WB and 1:200 for IF, gift from J.G. Gleeson (Lee et al., 2012)), rabbit anti-EHD1 (1:200 for IF, gift from S. Caplan (Zhang et al., 2012)), rabbit anti-TTBK2 (1:500 for IF, HPA018113, sigma), rabbit anti-CP110 (1:1000 for WB and 1:200 for IF, as described (Chen et al., 2002)), rabbit anti-Cep97 (1:200 for IF, A301-945A, Bethyl), rabbit anti-Rabaptin5 (1:200 for IF, sc-15351, SantaCruz), rabbit anti-Rab11 (1:200 for IF, 71-5300, Invitrogen), rabbit anti-Talpid3 (1:1000 for WB and 1:200 for IF, as described (Kobayashi et al., 2014)), mouse anti-CPAP (1:500 for IF, gift from T. Tang (Tang et al., 2009)), rabbit anti-CPAP (1:500 for IF, 11517-1-AP, Proteintech), rabbit anti-Ofd1 (1:2000 for WB and 1:500 for IF, gift from J.F. Reiter (Singla et al., 2010)), anti-Tctn1(1:100 for IF, 15004-1-AP, Proteintech, gift from J.F. Reiter), rabbit anti-Cep170 (1:500 for IF, A301-024A, Bethyl), rabbit anti-Usp33 (1:200 for IF, A300-925A, Bethyl), rabbit anti-Neurl4 (1:500 for IF, as described (Li et al., 2012)), rabbit anti-Kif24 (1:200 for IF, as described (Kobayashi et al., 2011)), rabbit anti-FBF1 (1:500 for IF, 11531-1-AP, Proteintech), rabbit anti-Cep83 (1:500 for IF, HPA038161, Sigma), rabbit anti-C2CD3 (1:500 for IF, HPA038552, Sigma), rabbit anti-Cep162 (1:500, HPA030170, sigma), rabbit anti-Cep164 (1:500 for IF, 45330002, Novus), rabbit anti-Arl1 (1:500 for IF, 16012-1-AP, Proteintech), mouse anti-β-actin (1:500 for IF, ab6276, Abcam), and mouse anti-β-catenin (1:500 for IF, C7207, Sigma).

Cell culture, drug treatment, and transferrin uptake assay

All cells were cultured at 37°C under 5% (vol/vol) CO_2. Human hTERT-RPE1 and HEK293T cells from the American Type Culture Collection (ATCC) were grown in DMEM supplemented with 10% (vol/vol) fetal bovine serum (FBS). Cells were switched to DMEM for serum-starvation.

The smoothened agonist SAG (Millipore) was added at 200 nM to induce Hedgehog pathway activation, Cytochalasin D (sigma) was used at 0.1 μg/ml to 10 μg/ml as indicated. Y-27632 (Cayman Chemical) was used at 25 μM. For transferrin uptake assay, serum-starved cells were treated with 10 μg/ml Texas-red-conjugated transferrin (Life Technologies) for 30 min. After washing with PBS, the cells were fixed with 10% formalin followed by immunofluorescence.

RNAi-mediated knock-down

All siRNAs were synthesized by Dharmacon, and Lipofectamine RNAiMAX (Invitrogen) was used for siRNA transfection according to the manufacturer's instructions. The sequence for non-specific control siRNA was 5'-AATTCTCCGAACGTGTCACGT-3' (Li et al., 2013). The two different Wdr35 siRNA oligos, a and b, were 5'-GAGAUACAGUCUACCUAAU-3', and 5'-UGAAGUGGGCCAAAGAUAA-3', respectively. SiRNA pools against IFT43 (M-015150-01, Dharmacon) and IFT144 (M-016094-02, Dharmacon) were purchased. Cep290 (5'-AAATTAAGATGCTCACCGATT-3') and Talpid3 (5'-CAAAGTTACCTACGTGTTATT-3') siRNAs were as described (Kobayashi et al., 2014). The siRNA sequence for PCM1 was 5'-GGCUUUAACUAAUUAUGGA-3' as described (Villumsen et al., 2013). The siRNA sequence for ACTR3 was 5'-GGACGAGAUAUAACAUAUU-3' as described (Kim et al., 2010).

Transfection, retrovirus infection and lentivirus infection

Polyethylenimine (PEI) was used for plasmid transfection in 293T cells. DNA and PEI (1 mg/ml) were added at 1:5 to 1:8 ratio. Lipofectamine 2000, 3000, or LTX was used for plasmid transfection in RPE1 cells according to the manufacturer's instructions.

Retroviral supernatant was prepared by transfection of the retroviral plasmids into Phoenix Amphotropic packaging cell line with PEI. Lentiviral supernatant was prepared by co-transfection of the lentiviral plasmid with Δ8.2 envelope and VsVG packaging plasmids into 293T cells using PEI. Both retrovirus and lentivirus supernatant were harvested 48-72 h post-transfection and filtered to remove the cell debris. 293T or RPE1 cells were incubated with virus supernatants in the presence of 8 μg/mL polybrene for 6 to 24 h, and medium was changed afterwards.

RNA isolation and quantitative real-time PCR

RNA isolation and quantitative real-time PCR were performed as previously described (Fu et al., 2014). TRIzol (Invitrogen) was used to isolate total RNA according the manufacturer's instructions. Verso cDNA synthesis kit (Thermo Scientific) was used for reverse transcriptase reaction. qRT-PCR analysis using the SYBR green method was performed, and relative gene expression was analyzed by ΔΔCt method. GAPDH was used as the reference gene.

Immunoprecipitation

Immunoprecipitations (IPs) were performed as described (Kim et al., 2015) with minor modifications. In

brief, cells were lysed with E1A lysis buffer (ELB) (50 mM Hepes/pH 7, 150 mM NaCl, 5 mM EDTA/pH 8, 0.1% NP-40, 1 mM dithiothreitol (DTT), 0.5 mM 4-(2-aminoethyl)benzenesulfonyl fluoride hydrochloride (AEBSF), 2 μg/ml leupeptin, 2 μg/ml aprotinin and 10% glycerol). For Flag immunoprecipitations, Flag-M2 beads (A2220, Sigma) were incubated with the cleared supernatants for at least 3 h, and the beads were washed with ELB buffer prior to analysis by SDS-PAGE and Western blotting. Similarly, anti-GFP antibody-bound Protein A or G beads were incubated with the lysates and processed as described above.

Immunofluorescence

Immunofluorescence was performed as previously described(Fu et al., 2014). Cells grown on coverslips were fixed with cold methanol at −20°C for 5 min. Alternatively, cells were fixed with 10% neutral buffered formalin (HT5014, Sigma) at room temperature for 15 min and extracted with PBS containing 0.2% (vol/vol) Triton X-10 for 5 min before being processed for immunofluorescence. Both the primary and secondary antibodies were diluted in PBS/3% (wt/vol) BSA/0.1% (vol/vol) Triton X-100. The coverslips were incubated with primary antibodies for 1 to 2 h at room temperature, washed in PBS and then incubated with secondary antibodies for at least 1 h at room temperature. Coverslips were washed with PBS and incubated with 0.1-1 μg/mL DAPI. Finally, cells were mounted with ProLong Gold Antifade reagent (Life Technologies) for microscopic analysis.

Microscopic analysis

For immunofluorescence microscopy, an Axiovert 200M microscope (Carl Zeiss) equipped with MetaMorph7 program (Molecular Devices) was used to acquire images. Alternatively, an LSM 800 confocal microscope (Zeiss) with Zen software (Zeiss) was used. ImageJ software was used for quantification and measurement of immunofluorescence images. Fiji package of ImageJ with Coloc2 plugin was used to evaluate protein co-localization (Schindelin et al., 2012). A Pearson's correlation coefficient ranging from -1 to 1 was used to score the co-localization, where 1 stands for perfect positive correlation, 0 for no correlation, and -1 for negative correlation. Regions encompassing the cilium were excluded to determine Arl13b and actin co-localization during measurement.

For live-cell imaging, RPE1 cells expressing fluorescence markers were plated in glass-bottom dishes or chamber slides. Data were acquired with an LSM 800 confocal microscope (Zeiss) with live imaging system. Bleaching in FRAP experiments was performed using a 488 nm laser, and the Fiji package was used for later analysis. Time-lapse movies were created using both Zen (Zeiss) and Corel VideoStudo (Ulead) software packages.

For transmission electron microscopy, the samples on grids were processed as described (Kim et al., 2015). An electron microscope (model CM-12; Philips/FEI) equipped with a 4-k × 2.7-k digital camera (Gatan, Inc.) was used to examine the stained grids.

Quantification and Statistical Analyses

All quantifications are based on a minimum of two or three independent experiments as indicated. A two-tailed Student's t-test was used to measure the statistical significance of differences of two groups. One-way ANOVA (analysis of variance) with post-hoc Tukey's test was used to compare multiple groups. $P < 0.05$ was considered significantly different.

Supplemental References

Arts, H.H., Bongers, E.M., Mans, D.A., van Beersum, S.E., Oud, M.M., Bolat, E., Spruijt, L., Cornelissen, E.A., Schuurs-Hoeijmakers, J.H., de Leeuw, N., *et al.* (2011). C14ORF179 encoding IFT43 is mutated in Sensenbrenner syndrome. Journal of medical genetics *48*, 390-395.

Avidor-Reiss, T., Maer, A.M., Koundakjian, E., Polyanovsky, A., Keil, T., Subramaniam, S., and Zuker, C.S. (2004). Decoding cilia function: defining specialized genes required for compartmentalized cilia biogenesis. Cell *117*, 527-539.

Balmer, S., Dussert, A., Collu, G.M., Benitez, E., Iomini, C., and Mlodzik, M. (2015). Components of Intraflagellar Transport Complex A Function Independently of the Cilium to Regulate Canonical Wnt Signaling in Drosophila. Developmental cell *34*, 705-718.

Behal, R.H., Miller, M.S., Qin, H., Lucker, B.F., Jones, A., and Cole, D.G. (2012). Subunit interactions and organization of the Chlamydomonas reinhardtii intraflagellar transport complex A proteins. The Journal of biological chemistry *287*, 11689-11703.

Bhogaraju, S., Engel, B.D., and Lorentzen, E. (2013). Intraflagellar transport complex structure and cargo interactions. Cilia *2*, 10.

Cevik, S., Sanders, A.A., Van Wijk, E., Boldt, K., Clarke, L., van Reeuwijk, J., Hori, Y., Horn, N., Hetterschijt, L., Wdowicz, A., *et al.* (2013). Active transport and diffusion barriers restrict Joubert Syndrome-associated ARL13B/ARL-13 to an Inv-like ciliary membrane subdomain. PLoS genetics *9*, e1003977.

Chavez, M., Ena, S., Van Sande, J., de Kerchove d'Exaerde, A., Schurmans, S., and Schiffmann, S.N. (2015). Modulation of Ciliary Phosphoinositide Content Regulates Trafficking and Sonic Hedgehog Signaling Output. Developmental cell *34*, 338-350.

Chen, Z., Indjeian, V.B., McManus, M., Wang, L., and Dynlacht, B.D. (2002). CP110, a cell cycle-dependent CDK substrate, regulates centrosome duplication in human cells. Developmental cell *3*, 339-350.

Chiba, S., Amagai, Y., Homma, Y., Fukuda, M., and Mizuno, K. (2013). NDR2-mediated Rabin8 phosphorylation is crucial for ciliogenesis by switching binding specificity from phosphatidylserine to Sec15. The EMBO journal *32*, 874-885.

Corbit, K.C., Aanstad, P., Singla, V., Norman, A.R., Stainier, D.Y., and Reiter, J.F. (2005). Vertebrate Smoothened functions at the primary cilium. Nature *437*, 1018-1021.

Davis, E.E., Zhang, Q., Liu, Q., Diplas, B.H., Davey, L.M., Hartley, J., Stoetzel, C., Szymanska, K., Ramaswami, G., Logan, C.V., *et al.* (2011). TTC21B contributes both causal and modifying alleles across the ciliopathy spectrum. Nature genetics *43*, 189-196.

Dodonova, S.O., Diestelkoetter-Bachert, P., von Appen, A., Hagen, W.J., Beck, R., Beck, M., Wieland, F., and Briggs, J.A. (2015). VESICULAR TRANSPORT. A structure of the COPI coat and the role of coat proteins in membrane vesicle assembly. Science *349*, 195-198.

Eugster, A., Frigerio, G., Dale, M., and Duden, R. (2004). The alpha- and beta'-COP WD40 domains mediate cargo-selective interactions with distinct di-lysine motifs. Molecular biology of the cell *15*, 1011-1023.

Fu, W., Asp, P., Canter, B., and Dynlacht, B.D. (2014). Primary cilia control hedgehog signaling during muscle differentiation and are deregulated in rhabdomyosarcoma. Proceedings of the National Academy of Sciences of the United States of America *111*, 9151-9156.

Garcia-Gonzalo, F.R., Phua, S.C., Roberson, E.C., Garcia, G., 3rd, Abedin, M., Schurmans, S., Inoue, T., and Reiter, J.F. (2015). Phosphoinositides Regulate Ciliary Protein Trafficking to Modulate Hedgehog Signaling. Developmental cell *34*, 400-409.

Gotthardt, K., Lokaj, M., Koerner, C., Falk, N., Giessl, A., and Wittinghofer, A. (2015). A G-protein activation cascade from Arl13B to Arl3 and implications for ciliary targeting of lipidated proteins. eLife *4*.

Hattula, K., Furuhjelm, J., Tikkanen, J., Tanhuanpaa, K., Laakkonen, P., and Peranen, J. (2006). Characterization of the Rab8-specific membrane traffic route linked to protrusion formation. Journal of cell science *119*, 4866-4877.

Hori, Y., Kobayashi, T., Kikko, Y., Kontani, K., and Katada, T. (2008). Domain architecture of the atypical Arf-family GTPase Arl13b involved in cilia formation. Biochemical and biophysical research communications *373*, 119-124.

Humbert, M.C., Weihbrecht, K., Searby, C.C., Li, Y., Pope, R.M., Sheffield, V.C., and Seo, S. (2012). ARL13B, PDE6D, and CEP164 form a functional network for INPP5E ciliary targeting. Proceedings of the National Academy of Sciences of the United States of America *109*, 19691-19696.

Jekely, G., and Arendt, D. (2006). Evolution of intraflagellar transport from coated vesicles and autogenous origin of the eukaryotic cilium. BioEssays : news and reviews in molecular, cellular and developmental biology *28*, 191-198.

Jin, H., White, S.R., Shida, T., Schulz, S., Aguiar, M., Gygi, S.P., Bazan, J.F., and Nachury, M.V. (2010). The conserved Bardet-Biedl syndrome proteins assemble a coat that traffics membrane proteins to cilia. Cell *141*, 1208-1219.

Kim, J., Lee, J.E., Heynen-Genel, S., Suyama, E., Ono, K., Lee, K., Ideker, T., Aza-Blanc, P., and Gleeson, J.G. (2010). Functional genomic screen for modulators of ciliogenesis and cilium length. Nature *464*, 1048-1051.

Kim, K., Lee, K., and Rhee, K. (2012). CEP90 is required for the assembly and centrosomal accumulation of centriolar satellites, which is essential for primary cilia formation. PloS one *7*, e48196.

Kim, S., Lee, K., Choi, J.H., Ringstad, N., and Dynlacht, B.D. (2015). Nek2 activation of Kif24 ensures cilium disassembly during the cell cycle. Nature communications *6*, 8087.

Kobayashi, T., Kim, S., Lin, Y.C., Inoue, T., and Dynlacht, B.D. (2014). The CP110-interacting proteins Talpid3 and Cep290 play overlapping and distinct roles in cilia assembly. The Journal of cell biology *204*, 215-229.

Kobayashi, T., Tsang, W.Y., Li, J., Lane, W., and Dynlacht, B.D. (2011). Centriolar kinesin Kif24 interacts with CP110 to remodel microtubules and regulate ciliogenesis. Cell *145*, 914-925.

Leaf, A., and Von Zastrow, M. (2015). Dopamine receptors reveal an essential role of IFT-B, KIF17, and Rab23 in delivering specific receptors to primary cilia. eLife *4*.

Lechtreck, K.F., Brown, J.M., Sampaio, J.L., Craft, J.M., Shevchenko, A., Evans, J.E., and Witman, G.B. (2013). Cycling of the signaling protein phospholipase D through cilia requires the BBSome only for the export phase. The Journal of cell biology *201*, 249-261.

Lechtreck, K.F., Johnson, E.C., Sakai, T., Cochran, D., Ballif, B.A., Rush, J., Pazour, G.J., Ikebe, M., and Witman, G.B. (2009). The Chlamydomonas reinhardtii BBSome is an IFT cargo required for export of specific signaling proteins from flagella. The Journal of cell biology *187*, 1117-1132.

Lee, C., and Goldberg, J. (2010). Structure of coatomer cage proteins and the relationship among COPI, COPII, and clathrin vesicle coats. Cell *142*, 123-132.

Lee, J.E., Silhavy, J.L., Zaki, M.S., Schroth, J., Bielas, S.L., Marsh, S.E., Olvera, J., Brancati, F., Iannicelli, M., Ikegami, K., *et al.* (2012). CEP41 is mutated in Joubert syndrome and is required for tubulin glutamylation at the cilium. Nature genetics *44*, 193-199.

Li, J., D'Angiolella, V., Seeley, E.S., Kim, S., Kobayashi, T., Fu, W., Campos, E.I., Pagano, M., and Dynlacht, B.D. (2013). USP33 regulates centrosome biogenesis via deubiquitination of the centriolar protein CP110. Nature *495*, 255-259.

Li, J., Kim, S., Kobayashi, T., Liang, F.X., Korzeniewski, N., Duensing, S., and Dynlacht, B.D. (2012). Neurl4, a novel daughter centriole protein, prevents formation of ectopic microtubule organizing centres. EMBO reports *13*, 547-553.

Liem, K.F., Jr., Ashe, A., He, M., Satir, P., Moran, J., Beier, D., Wicking, C., and Anderson, K.V. (2012). The IFT-A complex regulates Shh signaling through cilia structure and membrane protein trafficking. The Journal of cell biology *197*, 789-800.

Mill, P., Lockhart, P.J., Fitzpatrick, E., Mountford, H.S., Hall, E.A., Reijns, M.A., Keighren, M., Bahlo, M., Bromhead, C.J., Budd, P., *et al.* (2011). Human and mouse mutations in WDR35 cause short-rib polydactyly syndromes due to abnormal ciliogenesis. American journal of human genetics *88*, 508-515.

Mukhopadhyay, S., Wen, X., Chih, B., Nelson, C.D., Lane, W.S., Scales, S.J., and Jackson, P.K. (2010). TULP3 bridges the IFT-A complex and membrane phosphoinositides to promote trafficking of G protein-coupled receptors into primary cilia. Genes & development *24*, 2180-2193.

Mukhopadhyay, S., Wen, X., Ratti, N., Loktev, A., Rangell, L., Scales, S.J., and Jackson, P.K. (2013). The ciliary G-protein-coupled receptor Gpr161 negatively regulates the Sonic hedgehog pathway via cAMP signaling. Cell *152*, 210-223.

Prekeris, R. (2015). Analyzing the functions of Rab11-effector proteins during cell division. Methods in cell biology *130*, 19-34.

Qin, J., Lin, Y., Norman, R.X., Ko, H.W., and Eggenschwiler, J.T. (2011). Intraflagellar transport protein

122 antagonizes Sonic Hedgehog signaling and controls ciliary localization of pathway components. Proceedings of the National Academy of Sciences of the United States of America *108*, 1456-1461.

Sanjana, N.E., Shalem, O., and Zhang, F. (2014). Improved vectors and genome-wide libraries for CRISPR screening. Nature methods *11*, 783-784.

Schindelin, J., Arganda-Carreras, I., Frise, E., Kaynig, V., Longair, M., Pietzsch, T., Preibisch, S., Rueden, C., Saalfeld, S., Schmid, B., *et al.* (2012). Fiji: an open-source platform for biological-image analysis. Nature methods *9*, 676-682.

Singla, V., Romaguera-Ros, M., Garcia-Verdugo, J.M., and Reiter, J.F. (2010). Ofd1, a human disease gene, regulates the length and distal structure of centrioles. Developmental cell *18*, 410-424.

Su, S., Phua, S.C., DeRose, R., Chiba, S., Narita, K., Kalugin, P.N., Katada, T., Kontani, K., Takeda, S., and Inoue, T. (2013). Genetically encoded calcium indicator illuminates calcium dynamics in primary cilia. Nature methods *10*, 1105-1107.

Tang, C.J., Fu, R.H., Wu, K.S., Hsu, W.B., and Tang, T.K. (2009). CPAP is a cell-cycle regulated protein that controls centriole length. Nature cell biology *11*, 825-831.

Taschner, M., Bhogaraju, S., and Lorentzen, E. (2012). Architecture and function of IFT complex proteins in ciliogenesis. Differentiation; research in biological diversity *83*, S12-22.

van Dam, T.J., Townsend, M.J., Turk, M., Schlessinger, A., Sali, A., Field, M.C., and Huynen, M.A. (2013). Evolution of modular intraflagellar transport from a coatomer-like progenitor. Proceedings of the National Academy of Sciences of the United States of America *110*, 6943-6948.

Villumsen, B.H., Danielsen, J.R., Povlsen, L., Sylvestersen, K.B., Merdes, A., Beli, P., Yang, Y.G., Choudhary, C., Nielsen, M.L., Mailand, N., *et al.* (2013). A new cellular stress response that triggers centriolar satellite reorganization and ciliogenesis. The EMBO journal *32*, 3029-3040.

Wei, Q., Zhang, Y., Li, Y., Zhang, Q., Ling, K., and Hu, J. (2012). The BBSome controls IFT assembly and turnaround in cilia. Nature cell biology *14*, 950-957.

Williams, C.L., McIntyre, J.C., Norris, S.R., Jenkins, P.M., Zhang, L., Pei, Q., Verhey, K., and Martens, J.R. (2014). Direct evidence for BBSome-associated intraflagellar transport reveals distinct properties of native mammalian cilia. Nature communications *5*, 5813.

Wright, K.J., Baye, L.M., Olivier-Mason, A., Mukhopadhyay, S., Sang, L., Kwong, M., Wang, W., Pretorius, P.R., Sheffield, V.C., Sengupta, P., *et al.* (2011). An ARL3-UNC119-RP2 GTPase cycle targets myristoylated NPHP3 to the primary cilium. Genes & development *25*, 2347-2360.

Wu, V.M., Chen, S.C., Arkin, M.R., and Reiter, J.F. (2012). Small molecule inhibitors of Smoothened ciliary localization and ciliogenesis. Proceedings of the National Academy of Sciences of the United States of America *109*, 13644-13649.

Zhang, J., Reiling, C., Reinecke, J.B., Prislan, I., Marky, L.A., Sorgen, P.L., Naslavsky, N., and Caplan, S. (2012). Rabankyrin-5 interacts with EHD1 and Vps26 to regulate endocytic trafficking and retromer function. Traffic *13*, 745-757.